


## Article

# Numerical Simulation of the Negative Streamer Propagation Initiated by a Free Metallic Particle in N<sub>2</sub>/O<sub>2</sub> Mixtures under Non-Uniform Field

Bing Qi \*  and Daoxin Yu

Key Laboratory of Modern Power System Simulation and Control and Renewable Energy Technology, Ministry of Education, School of Electrical Engineering, Northeast Electric Power University, Jilin City 132012, China; yudaoxin1998@163.com

\* Correspondence: qibing@neepu.edu.cn

**Abstract:** Under atmospheric pressure, partial discharge initiated by free metallic particles has consistently been a significant factor leading to failures in high-voltage electrical equipment. Simulating the propagation of negative streamer discharge in N<sub>2</sub>/O<sub>2</sub> mixtures contributes to a better understanding of the occurrence and evolution of partial discharge, optimizing the insulation performance of electrical equipment. In this study, a two-dimensional plasma fluid dynamics model coupled with the current module was employed to simulate the evolution process of negative streamer discharge caused by one free metallic particle under a suspended potential at 220 kV applied voltage conditions. Simulation results indicated that the discharge process could be divided into two distinct stages: In the first stage, the electron ionization region detached from the electrode surface and propagated independently. During this stage, the corona discharge on the negative electrode surface provided seed electrons crucial for the subsequent development of negative corona discharge. The applied electric field played a dominant role in the propagation of the electron region, especially in the electron avalanche region. In the second stage, space charge gradually took over, causing distortion in the spatial field, particularly generating a substantial electric field gradient near the negative electrode surface, forming an ionization pattern dominated by ionization near the negative electrode surface. These simulation results contribute to a comprehensive understanding of the complex dynamic process of negative streamer discharge initiated by free metallic particles, providing essential insights for optimizing the design of electrical equipment and insulation systems.

**Keywords:** partial discharge; metallic particle; numerical simulation; negative streamer discharge



**Citation:** Qi, B.; Yu, D. Numerical Simulation of the Negative Streamer Propagation Initiated by a Free Metallic Particle in N<sub>2</sub>/O<sub>2</sub> Mixtures under Non-Uniform Field. *Processes* **2024**, *12*, 1554. <https://doi.org/10.3390/pr12081554>

Academic Editor: Masoud Soroush

Received: 3 July 2024

Revised: 18 July 2024

Accepted: 22 July 2024

Published: 25 July 2024



**Copyright:** © 2024 by the authors. Licensee MDPI, Basel, Switzerland. This article is an open access article distributed under the terms and conditions of the Creative Commons Attribution (CC BY) license (<https://creativecommons.org/licenses/by/4.0/>).

## 1. Introduction

As the voltage levels of high-voltage equipment continue to rise, power system failures caused by the adhesion of metallic particles have consistently been a crucial factor affecting system reliability. According to the Conseil International des Grands Réseaux Électriques (CIGRE) reports, up to 20% of insulation failures are related to particles and foreign objects [1]. Various types of foreign objects can be generated during the production, assembly, transportation, and operation of electrical equipment due to mechanical collisions, vibrations, and friction during plug-in contacts [2]. The open-field conditions in power equipment make surfaces prone to the accumulation of foreign particles, including millimeter-sized and micrometer-sized metallic particles, and even smaller. Particularly at accident sites, metallic particles adhering to the surfaces of equipment, mainly in millimeter sizes, are frequently discovered, along with a small portion of micrometer-sized and smaller metal dust particles. These particles may exist in direct contact or suspended states, leading to the gradual development of partial discharge and eventually evolving into flashovers. Hence, conducting a thorough investigation into the partial discharge phenomena triggered by free metallic particles is indispensable for comprehending the initiation and progression

of partial discharges. This comprehensive study is vital for improving the safety and reliability of power equipment. In this regard, the primary objective of the current research is to delve into the mechanisms underlying partial discharges induced by free metallic particles in power equipment. The findings of this study will offer robust support for system optimization and insulation design.

To gain a deeper understanding of the discharge evolution mechanisms involving suspended metallic particles, researchers have conducted a series of targeted experiments. These experiments have primarily focused on scenarios where metallic particles were present on insulator surfaces [3–5], metal shell surfaces [6–8], and in suspended or freely moving states [9–11]. In past studies, researchers have commonly utilized centimeter-sized metallic particles for ease of discharge signal detection [12,13]. However, the detection sensitivity limitations when dealing with millimeter-sized free metallic particles, commonly encountered in actual faults, often result in partial discharge signals exceeding the range of detection instruments. Furthermore, effective differentiation from noise is challenging, leading to a lack of detailed research on the partial discharge characteristics and discharge levels of millimeter-sized free metallic particles. Clearly, for better adaptation to real operating conditions, the study of partial discharge behavior in millimeter-sized free metallic particles holds significant importance. Additionally, partial discharge is a result of the comprehensive interaction of various processes, including charge generation and transport, energy transport of charges, excitation of molecules, and ionization processes. These processes form multiple discharge modes that interconvert with each other. Due to the limitations of measurement methods, macroscopic detection of electrical signals often hinders an in-depth analysis of discharge mechanisms. Consequently, experimental studies on discharge mechanisms face certain limitations. Overcoming these challenges will provide more comprehensive and accurate data for a profound understanding of the partial discharge mechanisms initiated by free metallic particles.

With the rapid development of computer technology, researchers increasingly favor the use of numerical simulation to delve into the mechanisms of microscale discharge processes. This research primarily focuses on the phenomenon of partial discharge inside Gas-Insulated Switchgear (GIS) [14–16] and Gas-Insulated Transmission Lines (GIL) [17–19], where such partial discharges are often caused by factors like voids, cracks, and metallic particles. Currently widely employed simulation methods include circuit model methods [20], Monte Carlo methods [21,22], multi-physics field coupling simulation methods [23,24], and plasma fluid models [25]. Among these, the plasma fluid model treats plasma as a continuous medium composed of electrons, ions, and neutral particles. Particularly at atmospheric pressure, it often satisfies the local thermodynamic equilibrium conditions well. This method can effectively simulate the evolution behavior of non-equilibrium plasma. The advantage of this model lies in its ability to more accurately reflect the changes in particles and energy of system components by considering excitation, adsorption, ionization, and recombination processes between electrons and heavy particles, involving the complex energy level structure of atoms and molecules. This makes it possible to better analyze the evolutionary patterns of the discharge process from a microscopic perspective. However, it is worth noting that this model introduces a large number of particle collision processes, significantly increasing computational complexity and posing challenges to the convergence of simulations. Overcoming these challenges will provide more accurate and efficient tools for simulation research, helping to reveal the microscopic mechanisms of partial discharge.

When free metallic particles come into contact with a high-voltage electrode or a grounded terminal, they acquire a fixed potential. This has a positive impact on simplifying the simulation process and enhancing the stability of the discharge. However, when metallic particles are located in other spatial positions, their potential changes accordingly. Metallic particles form a capacitance system with the surrounding medium, especially for millimeter-sized metallic particles, which can typically accommodate charge magnitudes on the order of picocoulombs [26]. This implies that once a partial discharge occurs, the

charging and discharging process will rapidly change the suspended potential of the metallic particles. Due to the extremely short time scale of this change, typically in the nanosecond range, partial discharge concludes within an extremely brief duration. This is also why measuring partial discharge signals initiated by metallic particles requires extremely high time resolution.

In this study, we successfully established a high-pressure partial discharge model in 80%N<sub>2</sub>/20%O<sub>2</sub> mixtures at atmospheric pressure, focusing on the behavior of a single metallic particle. As the metallic particle was suspended in the discharge space, a dual-head discharge mode, known as bipolar discharge, was generated. In this mode, the metallic particle formed a negative streamer discharge as the negative electrode toward the positive electrode. Simultaneously, the metallic particle acted as a positive electrode toward the negative direction, forming a positive streamer discharge. Both discharge modes coexisted. Through a detailed analysis of key parameters (such as electron density, electron temperature, and electric field) during the development and evolution of partial discharge in a single metallic particle, we aimed to gain a deeper understanding of the mechanisms underlying the occurrence and development of partial discharge. It is important to emphasize that this paper only explores the negative streamer discharge mode where the metallic particle discharges toward the positive electrode. This specific discharge mode may have significant implications in practical systems, and thus, we have provided a thorough discussion and analysis of it. Future research can further expand to comprehensively understand the diversity and complexity of partial discharge phenomena initiated by metallic particles. The simulation results in this paper align well with the already published experimental findings [27,28].

## 2. Numerical Model for Partial Discharge

### 2.1. Electrode System

The two-dimensional space for the discharge was set at 40 mm × 80 mm. The suspended metallic particle is illustrated in Figure 1. A voltage of 220 kV was applied to the upper boundary through metal contact, the lower boundary was grounded, the left boundary was insulated, and the right boundary was set as an open space cutoff. For generality, the metallic particles were chosen to have an elliptical shape with major and minor axes of 1 mm and 0.2 mm, respectively, placed at a distance of 2.5 mm from the upper electrode. The surface potential of the metallic particles was set as the suspended potential, determined by calculating the charging and discharging currents during the discharge process. To improve the convergence of the solution during calculations, the mesh near the metallic particles was refined, and the maximum step size of the solver was set to 10<sup>-4</sup> ns. The model neglected the influence of air components such as water vapor and carbon dioxide. A mixture of 20% oxygen and 80% nitrogen, representing a standard atmospheric pressure, was selected as the working gas.

The finite element modeling was conducted using the COMSOL 6.1 software. The meshing area was a freely distributed triangular network with an extremely refined division standard, and the meshes of the tip and streamer regions were further refined. A total of 414,306 meshing units was divided. The initial concentrations of electrons and positive ions were set to 10<sup>13</sup> m<sup>-3</sup>, and the initial concentration of negative ions was 0 m<sup>-3</sup>. The initial voltage of the electrostatic field was set to 0 V. For the transient process of the streamer, the automatic highly nonlinear Newton algorithm was adopted. In the solution process, the simulation step size was adaptive, which means that the solver automatically adjusted the calculation step size according to the solution process.

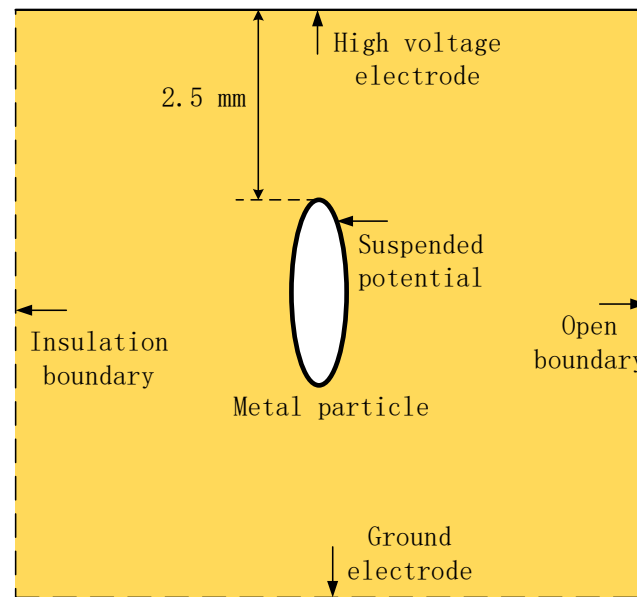


**Figure 1.** Schematic diagram of the two-dimensional simulation space model for one free metallic particle.

## 2.2. Fluid Simulation

The fluid model considers the plasma formed by partial discharge as a continuous medium composed of electrons, ions, and neutral particles, and describes them through the concentration, average velocity, and average energy of the particles. The continuity equation, momentum equation, and energy equation extracted from the Boltzmann equation were employed to obtain parameters for these particles. The Poisson equation was coupled with the aforementioned equations to obtain a self-consistent spatial distribution of the electric potential.

The expression for the continuity equation is as follows:

$$\frac{\partial n_{e,i}}{\partial t} + \nabla \cdot \Gamma_{e,i} = S_{e,i} \quad (1)$$

Here,  $e$  and  $i$  represent electrons and ions, respectively.  $t$  is time,  $n_{e,i}$  is the particle number density, and  $\Gamma_{e,i}$  is the particle flux, obtained through the transport diffusion equation.  $S_{e,i}$  represents the source term for particles.

The expression for the transport diffusion equation is as follows:

$$\Gamma_{e,i} = \mp q_{e,i} n_{e,i} \mu_{e,i} \mathbf{E} - D_{e,i} \nabla n_{e,i} \quad (2)$$

where  $q_{e,i}$  is the charge of the charged particles,  $\mu_{e,i}$  is the mobility of the charged particles,  $\mathbf{E}$  is the electric field strength, and  $D_{e,i}$  is the diffusion coefficient of the charged particles.

The source term  $S_{e,i}$  can be expressed as:

$$S_{e,i} = \sum_{j=1}^M x_j k_j N_n n_e \quad (3)$$

where  $M$  is the total number of target particles, and  $x_j$  is the molar fraction of the  $j$ th target particle,  $k_j$  is the rate coefficient for reaction  $j$ , and  $N_n$  is the neutral particle density.

The rate coefficients can be computed from cross-section data by the following integral:

$$k_j = \gamma \int_0^{\infty} \varepsilon \sigma_k(\varepsilon) f(\varepsilon) d\varepsilon \quad (4)$$

where  $\gamma = (2e/m_e)^{1/2}$ ,  $\varepsilon$  is the electron energy,  $\sigma_k$  is the collision cross section, and  $f(\varepsilon)$  is the electron energy distribution function (EEDF). In this case, a Boltzmann two term approximate electron temperature distribution function was assumed.

The acquisition of electron temperature requires solving the electron energy conservation equation:

$$\frac{\partial n_\varepsilon}{\partial t} + \nabla \cdot \Gamma_\varepsilon = S_{T_e} \quad (5)$$

where  $n_\varepsilon = n_e \bar{\varepsilon}$  represents the electron energy density,  $\bar{\varepsilon}$  is the average electron energy, and  $\Gamma_{\varepsilon-\varepsilon}$  is the electron energy flux density, expressed as follows:

$$\Gamma_\varepsilon = \frac{5}{3} n_e \mu_e \mathbf{E} - \frac{5}{3} D_e \nabla n_e \quad (6)$$

$S_{T_e}$  is the source term for electron energy, expressed as:

$$S_{T_e} = -e \Gamma_e \cdot \mathbf{E} - \sum_j \Delta E_j R_{inel,j} - 3 \frac{m_e}{M} k_b n_e \gamma_{en} (T_e - T_g). \quad (7)$$

where  $\Delta E_j$  and  $R_{inel,j}$  represent the energy loss caused by elastic collisions and the corresponding reaction rate,  $m_e$  and  $M$  are the electron and neutral gas particle masses,  $k_b$  is the Boltzmann constant,  $\gamma_{en}$  is the collision frequency between electrons and neutral particles,  $T_e$  is the electron temperature, and  $T_g$  is the gas temperature.  $S_{T_e}$  consists of three parts: Joule heating generated by the electric field, non-elastic collision loss of energy between electrons and heavy particles, and elastic collision loss of energy.

The spatial potential distribution is influenced by both the applied electric field and the electric field generated by space charges. It can be described by the Poisson equation:

$$\nabla^2 \varnothing = -\frac{\rho}{\varepsilon_0 \varepsilon_r} \quad (8)$$

where  $\varnothing$  is the spatial potential,  $\varepsilon_0$  is the permittivity of free space, and  $\varepsilon_r$  is the relative permittivity.  $\rho$  represents the space charge density and can be described as:

$$\rho = q \left( \sum_{k=1}^N Z_k n_k - n_e \right). \quad (9)$$

where  $\rho$  is the space charge density;  $q$  represents the elementary charge;  $Z_k$  is the quantity of the charge which  $k$  takes;  $n_k$  is the density of  $k$ .

### 2.3. Physical Chemistry Equation

For a more accurate simulation, this study incorporated major reactions in nitrogen and oxygen into the model, including excitation, adsorption, ionization, and elastic collision processes, as shown in Table 1.

**Table 1.** List of reactions and the rate constants [29,30].

No.	Reactions	Rate Constant (s <sup>-1</sup> ), (m <sup>3</sup> s <sup>-1</sup> ), or (m <sup>6</sup> s <sup>-1</sup> )
R1	$e + N_2 \Rightarrow 2e + N_2^+$	$1 \times 10^{-16} \bar{E}^{1.9} e^{-14.6/\bar{E}}$
R2	$e + N \Rightarrow 2e + N^+$	$1.45 \times 10^{-17} \bar{E}^{2.58} e^{-8.54/\bar{E}}$
R3	$e + O_2 \Rightarrow 2O + e$	$2.03 \times 10^{-14} \bar{E}^{-0.1} e^{-8.47/\bar{E}}$
R4	$e + O_2 \Rightarrow O + ({}^1D)O + e$	$1.82 \times 10^{-14} \bar{E}^{-0.13} e^{-10.7/\bar{E}}$
R5	$e + O_2 \Rightarrow O_2^+ + 2e$	$9.54 \times 10^{-12} \bar{E}^{-1.05} e^{-55.6/\bar{E}}$
R6	$e + O_3 \Rightarrow O_2 + O + e$	$1.78 \times 10^{-12} \bar{E}^{-0.61} e^{-11.5/\bar{E}}$
R7	$e + O \Rightarrow O_2^+ + 2e$	$4.75 \times 10^{-15} \bar{E}^{-0.61} e^{-22.1/\bar{E}}$
R8	$e + N^+ + M \Rightarrow N + M$	$3.12 \times 10^{-35} / T_e^{0.5}$
R9	$e + N_2^+ \Rightarrow N + ({}^2D)N$	$1.5 \times 10^{-12} / T_e^{0.7}$
R10	$e + N_2 \Rightarrow N_2^+ + 2e$	$1.66 \times 10^{-12} / T_e^{0.5}$

Table 1. Cont.

No.	Reactions	Rate Constant (s <sup>-1</sup> ), (m <sup>3</sup> s <sup>-1</sup> ), or (m <sup>6</sup> s <sup>-1</sup> )
R11	$e + N_2^+ + M \Rightarrow N_2 + M$	$3.12 \times 10^{-35} / T_e^{1.5}$
R12	$e + N_3^+ \Rightarrow N_2 + N$	$3.46 \times 10^{-12} / T_e^{0.5}$
R13	$e + N_4^+ \Rightarrow 2N_2$	$4.73 \times 10^{-11} / T_e^{0.53}$
R14	$e + O^+ + M \Rightarrow O + M$	$3.12 \times 10^{-35} / T_e^{1.5}$
R15	$e + O_2^+ \Rightarrow 2O$	$1.68 \times 10^{-11} / T_e^{0.7}$
R16	$e + O_2^+ + M \Rightarrow O_2 + M$	$3.12 \times 10^{-35} / T_e^{1.5}$
R17	$e + O_4^+ \Rightarrow 2O_2$	$2.42 \times 10^{-11} / T_e^{0.5}$
R18	$e + N_2O^+ \Rightarrow N_2 + O$	$3.46 \times 10^{-12} / T_e^{0.5}$
R19	$e + NO^+ \Rightarrow N + O$	$1.07 \times 10^{-11} / T_e^{0.85}$
R20	$e + NO^+ + M \Rightarrow NO + M$	$3.12 \times 10^{-35} / T_e^{1.5}$
R21	$e + NO_2^+ \Rightarrow NO + O$	$3.46 \times 10^{-12} / T_e^{0.5}$
R22	$e + NO^+ \Rightarrow O + ({}^2D)N$	$1.5 \times 10^{-12} / T_e^{0.7}$
R23	$e + 2O_2 \Rightarrow O_2 + O_2^-$	$1.4 \times 10^{-41} T_g / T_e e^{-600/T_e} e^{-(700(T_e - T_g))/T_g T_e}$
R24	$e + O_2 + N_2 \Rightarrow N_2 + O_2^-$	$1.1 \times 10^{-43} (T_g / T_e)^2 e^{-70/T_e} e^{-(1500(T_e - T_g))/T_g T_e}$
R25	$e + O_2 \Rightarrow O + O^-$	$2.63 \times 10^{-16} \bar{E}^{-0.495} e^{-5.65/\bar{E}}$
R26	$e + O_2 \Rightarrow O_2^-$	$9.72 \times 10^{-15} \bar{E}^{1.62} e^{-14.2/\bar{E}}$
R27	$e + O_3 \Rightarrow O_2 + O^-$	$1 \times 10^{-17}$
R28	$e + O_3 \Rightarrow O + O_2^-$	$1 \times 10^{-15}$
R29	$N + O^- \Rightarrow NO + e$	$2.6 \times 10^{-16}$
R30	$N_2 + O^- \Rightarrow N_2O + e$	$1 \times 10^{-18}$
R31	$O + O^- \Rightarrow O_2 + e$	$1.4 \times 10^{-16}$
R32	$O_2 + O^- \Rightarrow O_3 + e$	$1 \times 10^{-18}$
R33	$O_3 + O^- \Rightarrow 2O_2 + e$	$3 \times 10^{-16}$
R34	$O_2^- + N_2 \Rightarrow N_2 + O_2 + e$	$1.9 \times 10^{-18} (T_g/300)^{0.5} e^{-(4990/T_g)}$
R35	$O + O_2^- \Rightarrow O_3 + e$	$1.5 \times 10^{-16}$
R36	$O_2 + O_2^- \Rightarrow 2O_2 + e$	$2.7 \times 10^{-16} (T_g/300)^{0.5} e^{-(5590/T_g)}$

### 3. Results and Discussion

The discharge diagram at 0.63 ns is shown in Figure 2. Due to the suspension of metallic particle in the discharge space, discharges occurred simultaneously at the upper and lower tips, referred to as dual-head discharge mode in some literature. At the upper tip, negative streamer discharge formed as the metallic particle was at a lower potential compared to the positive electrode. Conversely, at the lower tip, positive streamer discharge formed as the metallic particle was at a higher potential relative to the grounded electrode. To clearly illustrate the discharge process, different electron density color scales are used for the upper and lower parts, placed on opposite sides due to the 1–2 order of magnitude lower electron density in the upper part. Figure 3 shows the charging current of the metallic particle and the resulting fluctuation in suspended potential. It can be observed that the surface current in the upper part was small, with a current magnitude on the order of  $10^{-4}$  A. In contrast, the surface current in the lower part was larger, with a current magnitude on the order of  $10^{-2}$  A. The fluctuation in suspended potential during the discharge process was within 30 V, causing no significant impact on the discharge process.

The upper and lower parts of the discharge involved complex physical mechanisms, and this paper focused solely on the mechanism of the upper part of the discharge.

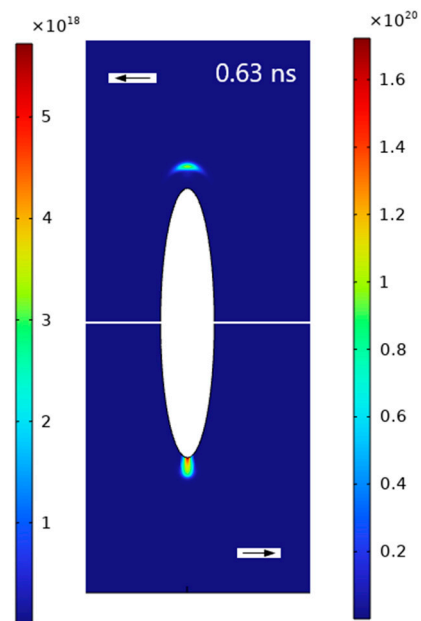


**Figure 2.** The electron density distribution map of the double-headed discharge around the suspended metallic particle. The color maps represent the electron density distribution, with the left side showing the color map for the upper half of the metallic particle and the right side for the lower half. The unit of electron density is  $\text{m}^{-3}$ .

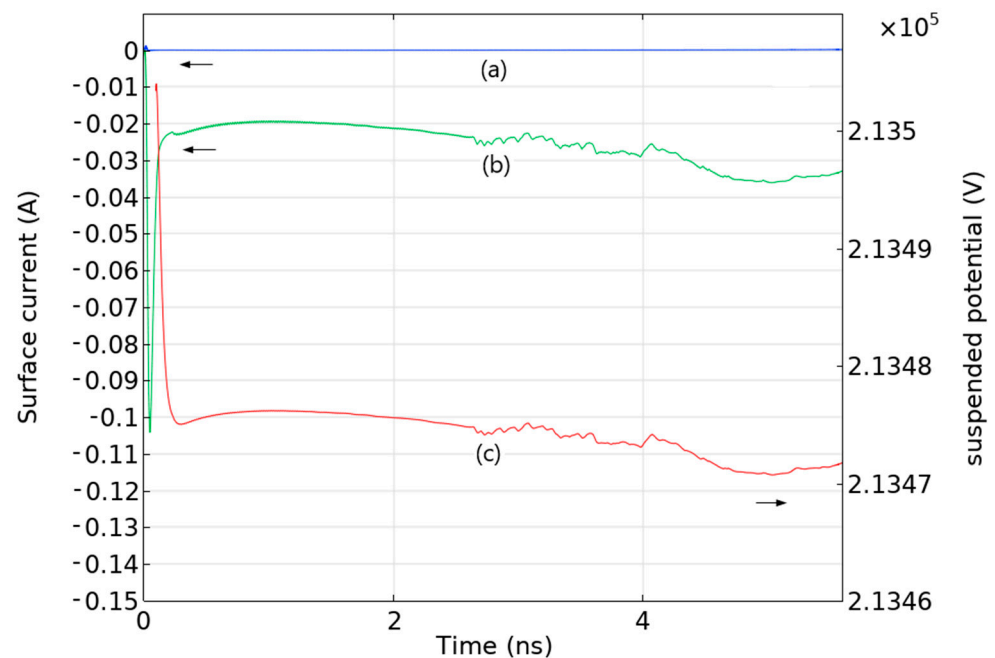


**Figure 3.** The charging and discharging currents on the surface of the metallic particle and the suspended potential. (a) Charging and discharging currents on the upper part, (b) charging and discharging currents on the lower part, and (c) surface suspended potential.

Figure 4 illustrates the electron propagation process during the streamer discharge of a free metallic particle toward the positive electrode under a 220 kV voltage. Due to the non-uniform distribution of the electric field at the tip of the metallic particle, the suspended potential was lower than the positive potential, resulting in a discharge mode known as



negative streamer discharge. Examining the electron propagation process revealed two distinct stages: The first stage, shown in Figure 4a–e, represents the initial phase of the discharge. Here, the electron density was on the order of  $10^{18} \text{ m}^{-3}$ , forming a “crescent” shape with high central density and low peripheral density. The electron region detached from the electrode surface and propagated toward the positive electrode at a speed ranging from  $1.6 \times 10^7$  to  $2.2 \times 10^7 \text{ cm}\cdot\text{s}^{-1}$ , with a slight increase in propagation speed as the distance grew. The second stage was the radial and axial expansion of electrons, as depicted in Figure 4f–j. During this phase, the electron density expanded simultaneously in the radial and axial directions, forming a “mushroom” shape. The head’s electron density gradually decreased, while the tail extended toward the negative electrode surface. Near the tail end, a high-density electron region gradually formed, with a maximum electron density reaching  $2.1 \times 10^{19} \text{ m}^{-3}$ , as shown in Figure 4j.

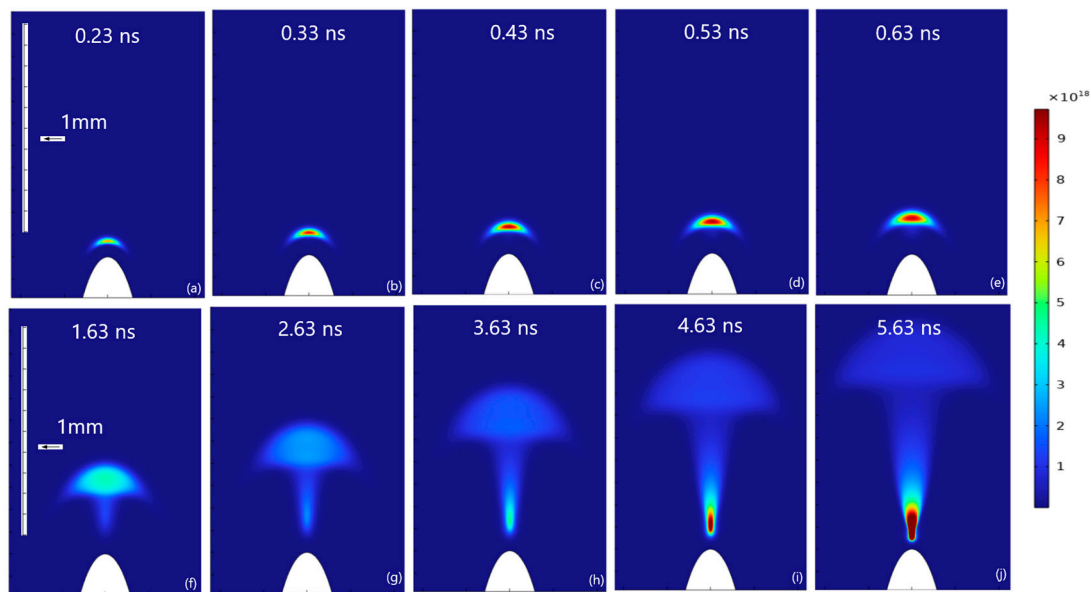


**Figure 4.** The development process of negative streamer discharge electron density. (a–e) represent the first stage of discharge development, while (f–j) represent the second stage of discharge development.

The first stage of axial electron density development along the axis is shown in Figure 5a. The axial distribution of electron density exhibits a single-peak structure, with the peak values increasing gradually from  $2.1 \times 10^{19} \text{ m}^{-3}$  at 0.23 ns to  $2.1 \times 10^{19} \text{ m}^{-3}$  at 0.53 ns and then gradually decreasing. From the figure, it can be observed that the development of the electron region is independent and moves forward, detached from the electrode surface area, corresponding to Figure 4a–e. The axial distribution of the electric field in Figure 6a shows that, at this stage, the applied electric field plays a dominant role, continuously propelling electrons forward. However, the electron density gradient and space charge remain secondary factors. As the propagation time increases, entering the second stage of development, as shown in Figure 5b, the axial distribution of electron density undergoes significant changes compared to the first stage. The electron density region expands simultaneously in both positive and negative directions. Due to the large amplitude of peak value changes at different times, the vertical axis in Figure 5b is represented exponentially. The electron density peak propagating toward the positive electrode gradually flattens, with the peak value decreasing, maintaining a propagation speed in the range of  $1.6 \times 10^7$  to  $2.2 \times 10^7 \text{ cm}\cdot\text{s}^{-1}$ , similar to the first stage. Meanwhile, the peak value of electron density propagating toward the negative electrode gradually increases from  $0.5 \times 10^{18} \text{ m}^{-3}$  at 1.63 ns to  $2.1 \times 10^{19} \text{ m}^{-3}$  at 5.63 ns. The peak propagation speed increases from  $2.3 \times 10^6 \text{ cm}\cdot\text{s}^{-1}$  at 1.63 ns to  $5.8 \times 10^6 \text{ cm}\cdot\text{s}^{-1}$  at 5.63 ns, being one order of magnitude lower compared to the propagation speed toward the positive electrode. Simultaneously, the peak value propagating toward the negative electrode increases rapidly,



while the peak value propagating toward the positive electrode gradually decreases. At 5.63 ns, the ratio between the two is as high as 61 times. This corresponds to the electron density distribution in the second stage of discharge shown in Figure 4f–j. The electric field distribution in Figure 6b indicates that near the negative electrode surface, a strong electric field dominates, where ionization mainly occurs, and the ionization-generated electrons form the electron density peak in this region. In contrast, the electron region propagating toward the positive electrode gradually decreases due to the weakening electric field.

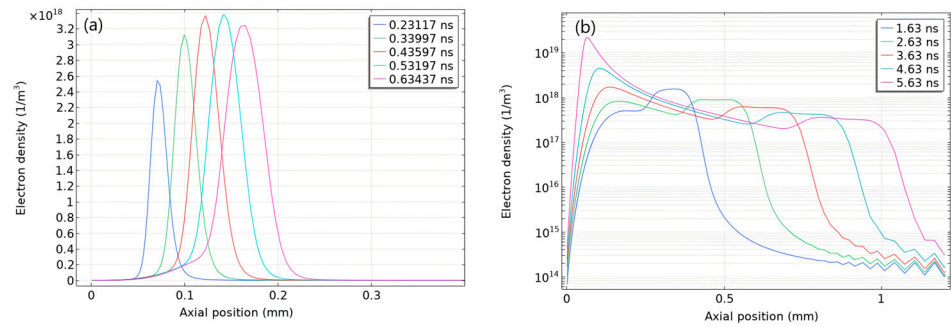


**Figure 5.** Axial electron density distribution. (a) Axial electron density distribution in the first stage of discharge, (b) Axial electron density distribution in the second stage, vertical axis represented in exponential scale.

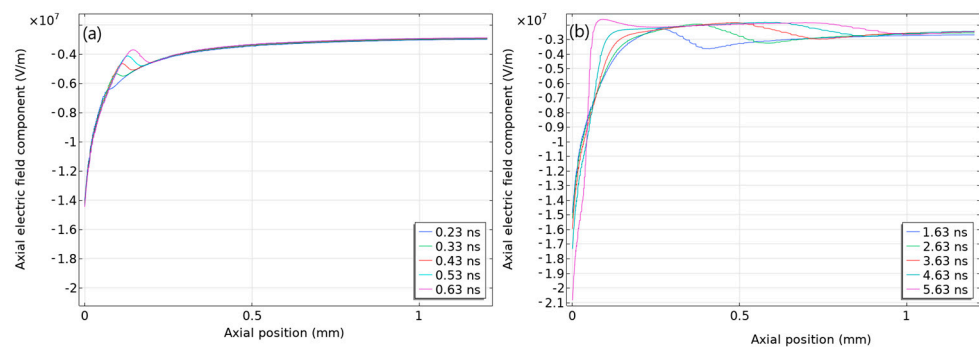


**Figure 6.** Axial distribution of the electric field component. (a) Distribution of electric field components in the first stage of discharge. (b) Distribution of electric field components in the second stage of discharge.

The axial distribution of positive ion density during the first stage of discharge is shown in Figure 7a. At 0.23 ns, there was a peak positive ion density of  $1.00 \times 10^{18} \text{ m}^{-3}$  in the electrode surface region, as shown in the magnified part of the figure. This peak gradually weakened over time and decreases to  $0.51 \times 10^{18} \text{ m}^{-3}$  at 0.63 ns, indicating a gradual reduction in the corona discharge at the negative electrode surface during the first stage of discharge. Another peak appeared in the region away from the negative electrode and gradually strengthened over time, reaching a maximum of  $2.27 \times 10^{18} \text{ m}^{-3}$  at 0.63 ns. It is noteworthy that, in comparison with the electron density in Figure 5a, the electron density reached its maximum peak at 0.53 ns, while the positive ion density continued to increase. This suggests that positive space charge gradually had a significant impact on the electric field after 0.53 ns. In the second stage of discharge, as seen in Figure 7b, the curves at different times almost overlapped on the right boundary, and the peak moved to the left with time. This indicates that the positive ion region expanded slowly toward the positive electrode and rapidly toward the negative electrode. The corresponding peak movement velocity was between  $1.0 \times 10^6$  and  $2.0 \times 10^6 \text{ cm} \cdot \text{s}^{-1}$ . This velocity was of the same order of magnitude as the movement velocity of the electron peak toward the negative electrode, indicating that the expansion of the electron density region toward the negative electrode is dominated by the space charge of positive ions.

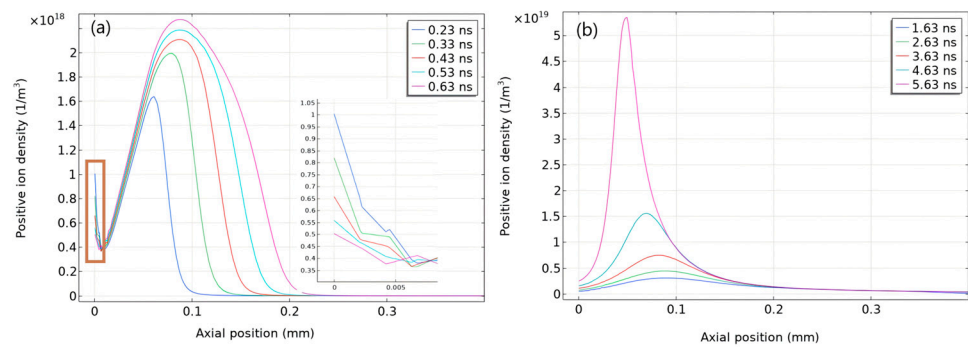


**Figure 7.** The axial distribution of positive ion density. The axial distribution of positive ion density during the first stage of discharge is shown in (a), with a magnified view of the boxed region on the right. (b) represents the axial distribution of positive ion density during the second stage of discharge.

$O_2$  and  $O_3$  adsorbed electrons through reactions R23–R28, exhibiting strong electronegativity. Figure 8a presents the axial distribution of negative ions during the first stage of discharge over time. From the magnified view on the negative electrode surface, it can be observed that after the formation of the negative corona on the negative electrode surface, the negative ion density peak in this area remained basically unchanged, only shifting forward overall with time. This indicates that after the formation of the negative corona on the negative electrode surface, the adsorption process of negative ions quickly ceased, and negative ions migrated forward under the influence of the electric field. This process was consistent with the formation process of positive ions on the negative electrode surface (Figure 8a). In the region slightly away from the negative electrode, a peak in negative ion density appeared. As shown in Figure 8a, the left side of the negative ion distribution curve in this region almost overlapped, and the peak coincided with the electron peak (Figure 5a), indicating that the formation of negative ions was associated with the electron ionization process. The negative ion density was on the order of  $10^{16} \text{ m}^{-3}$ , lower by 1–2 orders of magnitude than the electron density and ion density, and could not play a dominant role in the discharge process. In the second stage of discharge development, with the enhancement of the positive ion region near the negative electrode, the negative ion peak gradually moved toward the negative electrode, as shown in Figure 8b. The negative ion density was on the order of  $10^{16}$  to  $10^{18} \text{ m}^{-3}$ , still 1–2 orders of magnitude lower than the electron density and ion density at the same time, and could not play a dominant role in the discharge development process.

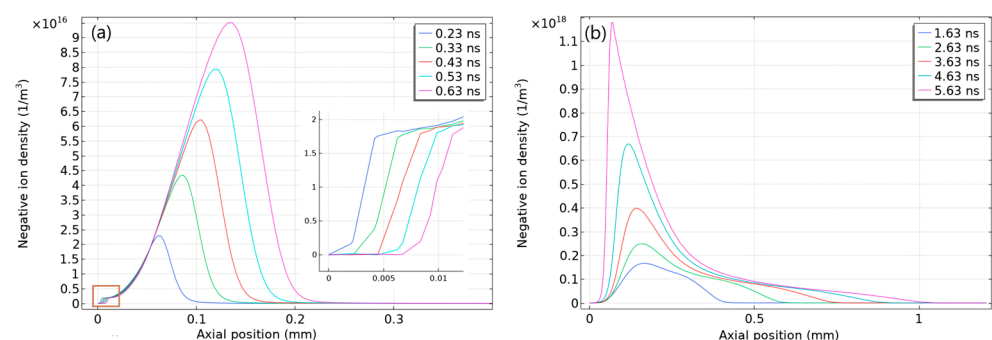


**Figure 8.** The axial distribution of negative ion density. The axial distribution of negative ion density during the first stage of discharge is shown in (a), and the enlarged view in the box on the right. (b) represents the axial distribution of negative ion density during the second stage of discharge.

The corona discharge on the negative electrode surface gradually weakened over time, and the positive space charge density gradually decreased, as shown in the magnified portion of Figure 9a. Combined with Figures 6a and 7a, it can be observed that the corona discharge played a crucial role throughout the entire discharge process. The seed electrons

generated by the corona discharge passed through the drift region, providing initial seed electrons for the downstream negative streamer discharge along the axial direction. The positive ion density region and the electron density region formed two independent regions, and at this point, the influence of the positive ion region on the axial propagation of electrons was minimal. The axial distribution of space charge during the second stage of discharge development is shown in Figure 9b. There was a significant change in the spatial charge distribution compared to the first stage. The positive ion density region rapidly intensified, reaching a peak space charge density of  $1.38 \times 10^{19} \text{ m}^{-3}$  at 4.63 ns, and moved toward the surface region of the negative electrode. Simultaneously, the electron density region expanded in both directions, and the peak gradually decreased. This indicates that, at this stage, positive space charge dominated the discharge process, controlling both the generation of electrons and the ionization process, with ionization primarily occurring in the surface region near the negative electrode.

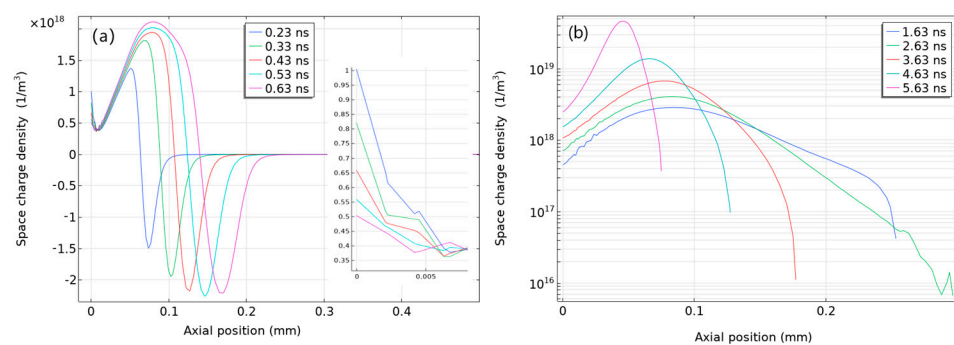


**Figure 9.** Axial distribution of space charge density. (a) Axial distribution of space charge density during the first stage of discharge, with a magnified view in the inset on the right. (b) Axial distribution of space charge density during the second stage of discharge.

In the first stage of discharge, as seen in the axial electric field distribution in Figure 6a, the appearance of space charge regions led to a decrease in the electric field strength between these regions, resulting in a weakening of the ionization process in this area. However, in the front part of the region where the electron zone propagated toward the anode, the electric field distribution was not affected, and the field remained relatively strong. This region propelled the ionization process continuously toward the anode, giving rise to the process of electrons detaching from the cathode and independently propagating forward, as shown in Figure 4a, forming the first stage of discharge. Due to the weakening of the external electric field with increasing distance and the simultaneous radial diffusion of the electron region, the electron density in the first stage gradually decreased after reaching its peak at 0.53 ns. The reduced electric field contour plot in Figure 10 also illustrates that at the initial stage of discharge (0.23 ns), the contour distribution formed concentric arcs centered around the cathode. As the discharge progressed, the central part of the contours gradually approached the cathode surface axially, while the shape of the contours in other areas remained relatively unchanged. Further into the discharge, at 5.63 ns, the contours near the cathode tip surface showed a significant spatial gradient, indicating drastic changes in the electric field in this region. Combined with Figure 6b, at 5.63 ns, the maximum electric field on the cathode surface reached  $-2.1 \times 10^7 \text{ V}\cdot\text{m}^{-1}$ , while the lowest field slightly further away reached  $1.6 \times 10^6 \text{ V}\cdot\text{m}^{-1}$ , differing by an order of magnitude. This resulted in the discharge area being mainly confined to the narrow axial region near the electrode surface in the second stage of discharge, as shown in Figure 4j.

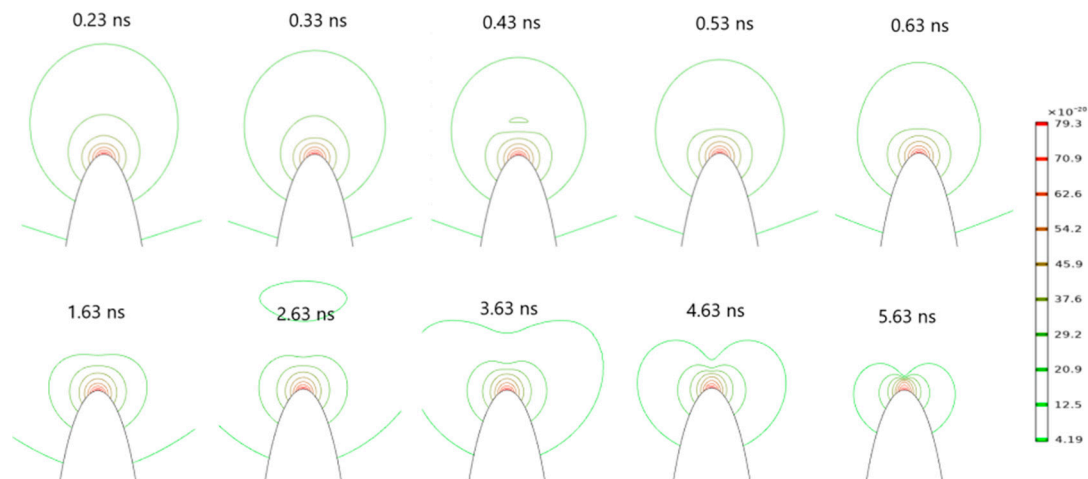


**Figure 10.** The two-dimensional evolution diagram of equipotential lines for the reduced electric field strength.

#### 4. Conclusions

This paper employed a two-dimensional plasma fluid dynamics model coupled with the electron collision reaction equation to investigate the evolutionary development of local discharge on free metallic particles in an 80%N<sub>2</sub>/20%O<sub>2</sub> mixed gas. In a high-voltage discharge device at 220 kV, elliptical free metallic particles exhibited a dual-head discharge mode, and this paper studied the local discharge development process of metallic particles toward the anode.

The research results indicate that the discharge process was clearly divided into two stages: The first stage of the discharge process began with the corona discharge on the surface of the metallic particles. The electrons generated by the corona discharge traversed the drift region and acted as seed electrons for the rear negative streamer discharge. At this stage, the negative streamer discharge was dominated by the external electric field, and the electron density region and ion density region exhibited a separated state. The electron density region propagated rapidly toward the anode axially, with a speed ranging from  $1.6 \times 10^7$  to  $2.2 \times 10^7$  V·m<sup>-1</sup>, while the electron density gradually diffused and weakened over time.

The second stage was characterized by the space charge electric field formed by positive ions gradually taking dominance in the discharge process. A peak positive ion density region formed near the cathode surface, triggering a stronger negative streamer discharge. The maximum electron density reached  $2.1 \times 10^{19}$  m<sup>-3</sup>, an order of magnitude higher than the electron density in the first stage. The contour plot of the reduced electric field distribution over time revealed non-uniform evolution in space, with stronger variations along the axial direction. The relatively low negative ion density had no decisive impact on the discharge development process.

In actual engineering, the geometry, position, and concentration of metallic particles in high-voltage equipment can vary significantly. Different particle geometries can have a significant impact on the discharge process and the conclusions of this study, as non-elliptical or irregularly shaped particles may lead to more complex electric field distributions, thereby affecting the initiation and propagation of the discharge. In addition, the position of the particles can affect the local electric field strength and the possibility of discharge occurrence, and a higher concentration of particles can increase the probability of interaction between them, further reducing the stability of the system. To improve the insulating equipment, further research is needed on the effects of different particle geometries, positions, and concentrations to develop more accurate models and design guidelines and improve the reliability and safety of high-voltage equipment. In general, this study provides insights into the discharge behavior of a single ideal elliptical particle, but more research is needed

to extend these findings to more realistic and complex scenarios in order to improve the design of high-voltage insulating equipment.

**Author Contributions:** Conceptualization, B.Q.; methodology, B.Q.; software, B.Q. and D.Y.; validation, B.Q. and D.Y.; formal analysis, D.Y.; writing—original draft preparation, B.Q.; writing—review and editing, B.Q.; funding acquisition, B.Q. All authors have read and agreed to the published version of the manuscript.

**Funding:** This research was funded by [Jilin Provincial Natural Science Foundation] grant number [20240101094]C] and The APC was funded by [Jilin Provincial Natural Science Foundation].

**Data Availability Statement:** Data are contained within the article.

**Conflicts of Interest:** The authors declare no conflict of interest.

## References

1. Sabot, A.; Koltunowicz, W.; Boeck, W. Insulation co-ordination of GIS: Return of experience, on site tests and diagnostic techniques. *Electra* **1998**, *176*, 67–95.
2. Budiman, F.N.; Khan, Y.; Khan, A.A.; Beroual, A.; Malik, N.H.; Al-Arainy, A.A. Dependence of Particle Initiated PD Characteristics on Size and Position of Metallic Particle Adhering to the Spacer Surface in GIS. *Waset Org.* **2013**, *7*, 349–353.
3. Inami, K.; Yoshida, T.; Hama, H.; Nakadai, Y.; Yamamoto, T. Partial Discharge and Breakdown Properties in Dry air, N<sub>2</sub>, CO<sub>2</sub> under Non-uniform Electric Field. *IEEE Trans. Dielectr. Electr. Insul.* **2023**, *30*, 2583–2591. [[CrossRef](#)]
4. Ren, M.; Dong, M.; Ye, R.; Liu, Y. Partial discharge test under standard oscillating impulses on a gas-insulated bus with artificial metal particle defects on the insulator surface. *IEEE Trans. Dielectr. Electr. Insul.* **2016**, *23*, 3593–3601. [[CrossRef](#)]
5. Li, X.; Liu, W.; Xu, Y.; Ding, D. Discharge Characteristics and Detectability of Metal Particles on the Spacer Surface in Gas-Insulated Switchgears. *IEEE Trans. Power Deliv.* **2022**, *37*, 187–196. [[CrossRef](#)]
6. Wang, Z.; Wang, R.X.; Gao, J.M.; Chen, K.; Liang, Y.J.; Tang, Z.Z. Reliability Prediction for GIL Equipment Based on Multilayer Directed and Weighted Network and Failure Propagation. *IEEE Trans. Reliab.* **2020**, *4*, 1207–1229. [[CrossRef](#)]
7. Vasantha Gowri, N.; Raju, M.R.; Singh, B.P. Occurrence of partial discharge induced by metal particles in high voltage transformer. In Proceedings of the 2015 North American Power Symposium (NAPS), Charlotte, NC, USA, 4–6 October 2015; pp. 1–6.
8. Shen, R.; Ou, Y.; Zhou, Y.; Zhao, W.; Li, X. Partial Discharge Detection and Characteristics of Gas-insulated Substation Free Metal Particles Based on Acoustic Emission. *Sens. Mater.* **2019**, *31*, 1467–1475. [[CrossRef](#)]
9. Wang, D.; Xin, W.; Chen, T.; Ma, D.; Fu, H.; Zhang, Z.; Zhang, S.; Lv, L. Multispectral characteristic analysis for free metallic particle discharge in SF<sub>6</sub> gas conditions. In Proceedings of the Third International Conference on Electronics, Electrical and Information Engineering (ICEEIE 2023), Xiamen, China, 11–13 August 2023; Volume 12922.
10. Wang, P.; Zhang, N.; Xu, J.; Zhang, J.; He, B. Charging Characteristics of Micrometer-Sized Metal Particles and Their Effects on Partial Discharge of Insulating Oil in Flowing. *IEEE Trans. Dielectr. Electr. Insul.* **2023**, *30*, 1145–1153. [[CrossRef](#)]
11. Shi, W.; Yang, Z.L.; Chen, H.X.; Lu, Z.W.; Wang, D.; Xin, W.F. Characteristic Analysis of Partial Discharge of Free Metal Particle in GIS. *IOP Conf. Ser. Earth Environ. Sci.* **2019**, *354*, 012121. [[CrossRef](#)]
12. Wang, J.; Li, Q.; Li, B.; Chen, C.; Liu, S.; Li, C. Theoretical and experimental studies of air gap breakdown triggered by free spherical conducting particles in DC uniform field. *IEEE Trans. Dielectr. Electr. Insul.* **2016**, *23*, 1951–1958. [[CrossRef](#)]
13. Färber, R.; Šefl, O.; Franck, C.M. On the influence of humidity on the breakdown strength of air—With a case study on the PDIV of contacting enameled wire pairs. *J. Phys. D Appl. Phys.* **2023**, *57*, 075202. [[CrossRef](#)]
14. Song, H.; Zhang, Z.; Tian, J.; Sheng, G.; Jiang, X. Multiscale Fusion Simulation of the Influence of Temperature on the Partial Discharge Signal of GIS Insulation Void Defects. *IEEE Trans. Power Deliv.* **2022**, *37*, 1304–1314. [[CrossRef](#)]
15. Han, X.; Li, J.; Sun, W.; Han, S. Simulation Study on Propagation Characteristics of Optical Signals Excited by Partial Discharge in GIS. In Proceedings of the 2020 IEEE International Conference on High Voltage Engineering and Application (ICHVE), Beijing, China, 6–10 September 2020; pp. 1–5.
16. Ma, J.; Chen, Y.; Zhang, X.; Zheng, Z.; Li, M. A Defect Model for Simulating Suspended Potential Discharge in GIS. In Proceedings of the 2021 4th International Conference on Energy, Electrical and Power Engineering (CEEPE), Chongqing, China, 23–25 April 2021; pp. 59–63.
17. Qin, X.; Zhao, H.; Zhang, Q.; Qian, Y.; Sheng, G.; Jiang, X. Simulation on Propagation Characteristics of Optical Signals of Partial Discharge in Single-core and Three-cores GIL. In Proceedings of the 2018 Condition Monitoring and Diagnosis (CMD), Perth, WA, Australia, 23–26 September 2018; pp. 195–198.
18. Vu-Cong, T.; Toigo, C.; Ortiz, G.; Dalstein, M.; Jacquier, F.; Girodet, A. Numerical simulation of partial discharge current pulse: Comparison between SF<sub>6</sub>, Fluoronitrile—CO<sub>2</sub> mixture and Fluoroketone—CO<sub>2</sub> mixture. In Proceedings of the 2020 IEEE Conference on Electrical Insulation and Dielectric Phenomena (CEIDP), East Rutherford, NJ, USA, 18–30 October 2020; pp. 725–728.



19. Toigo, C.; Vu-Cong, T.; Jacquier, F.; Girodet, A. Partial discharge behavior of protrusion on high voltage conductor in GIS/GIL under high voltage direct current: Comparison of SF<sub>6</sub> and SF<sub>6</sub> alternative gases. *IEEE Trans. Dielectr. Electr. Insul.* **2020**, *27*, 140–147. [[CrossRef](#)]
20. Yousaf, J.; Park, M.; Lee, H.; Youn, J.; Lee, D.; Hwang, C.; Nah, W. Efficient Circuit and an EM Model of an Electrostatic Discharge Generator. *IEEE Trans. Electromagn. Compat.* **2018**, *60*, 1078–1086. [[CrossRef](#)]
21. Settaouti, A.; Settaouti, L. Monte Carlo simulation of electrical corona discharge in air. *Electr. Power Syst. Res.* **2011**, *81*, 84–89. [[CrossRef](#)]
22. Marskar, R.; Meyer, H.K.H. A kinetic Monte Carlo study of positive streamer interaction with complex dielectric surfaces. *Plasma Sources Sci. Technol.* **2023**, *32*, 085010. [[CrossRef](#)]
23. Jovanović, A.P.; Stankov, M.N.; Loffhagen, D.; Becker, M.M. Automated Fluid Model Generation and Numerical Analysis of Dielectric Barrier Discharges Using Comsol. *IEEE Trans. Plasma Sci.* **2021**, *49*, 3710–3718. [[CrossRef](#)]
24. Sahu, A.; Sahoo, R.; Karmakar, S. The Study of Electric Field and Partial Discharges on XLPE Insulation under DC High Voltage using COMSOL Multiphysics. In Proceedings of the 2021 3rd International Conference on High Voltage Engineering and Power Systems (ICHVEPS), Bandung, Indonesia, 5–6 October 2021; pp. 1–5.
25. Liu, S.-H.; Trelles, J.P.; Murphy, A.B.; Li, L.; Zhang, S.-L.; Yang, G.-J.; Li, C.-X. Numerical simulation of the flow characteristics inside a novel plasma spray torch. *J. Phys. D Appl. Phys.* **2019**, *52*, 335203. [[CrossRef](#)]
26. Qi, B.; Li, C.; Hao, Z.; Geng, B.B.; Xu, D.G.; Liu, S.; Deng, C. Evolution phenomena and features of surface partial discharge initiated by immobilized metal particles on GIS insulators. *Proceeding CSEE* **2011**, *31*, 101–108.
27. Sarathi, R.; Umamaheswari, R. Understanding the partial discharge activity generated due to particle movement in a composite insulation under AC voltages. *Int. J. Electr. Power Energy Syst.* **2013**, *48*, 1–9. [[CrossRef](#)]
28. Sun, J.; Wu, N.; Fan, Y.; Lei, D.; Yang, S.; Guo, X.; Wang, H.; Song, S. Partial discharge characteristics of free moving metal particles in gas insulated systems under DC and AC voltages. *IET Gener. Transm. Distrib.* **2022**, *17*, 1047–1058. [[CrossRef](#)]
29. Kossyi, I.A.; Kostinsky, A.Y.; Matveyev, A.A.; Silakov, V.P. Kinetic scheme of the non-equilibrium discharge in nitrogen-oxygen mixtures. *Plasma Sources Sci. Technol.* **1992**, *1*, 207–220. [[CrossRef](#)]
30. Sakiyama, Y.; Graves, D.B.; Chang, H.W.; Shimizu, T.; Morfill, G.E. Plasma chemistry model of surface microdischarge in humid air and dynamics of reactive neutral species. *J. Phys. D Appl. Phys.* **2012**, *45*, 425201. [[CrossRef](#)]

**Disclaimer/Publisher’s Note:** The statements, opinions and data contained in all publications are solely those of the individual author(s) and contributor(s) and not of MDPI and/or the editor(s). MDPI and/or the editor(s) disclaim responsibility for any injury to people or property resulting from any ideas, methods, instructions or products referred to in the content.